Materials Advances

ROYAL SOCIETY OF CHEMISTRY

PAPER

View Article Online
View Journal

Cite this: DOI: 10.1039/d6ma00478d

Atomically engineered black phosphorene nanosheets for selective detection of ovarian cancer VOC biomarkers

D. Ramkumar, K. A. Jeeva Vergin Raj, N. Viveka, C. Preferencial Kala* and R. M. Hariharan

Early-stage diagnosis of ovarian cancer is critically limited by the absence of sensitive, non-invasive screening technologies. The analysis of disease-associated VOCs in exhaled breath is a promising diagnostic route; however, success depends on sensor materials that can differentiate chemically similar analytes with high precision. This work focuses on developing a nanoscale sensing platform with enhanced sensitivity and reliable selectivity for key ovarian cancer VOC biomarkers, including 2-butanone, decanal, and nonanal. To uncover the sensing mechanism and assess stability against interfering gases (H_2O and CO_2), we used van der Waals corrected DFT+NEGF transport calculations to analyse the adsorption behaviour and electronic response on metal-functionalized black phosphorene. We found that pristine black phosphorene interacts only weakly with the VOCs, exhibiting low adsorption energies (E_{ads}) that limit its practical sensing capability. In contrast, metal functionalization with Au, Ag, and Cu markedly enhances molecular binding. Among all configurations, Cu@BP shows the strongest affinity, with adsorption energies of −0.82 eV for 2-butanone, −0.68 eV for decanal, and −0.65 eV for nonanal, respectively. Charge-transport analysis demonstrates that Cu-decorated black phosphorene exhibits a markedly enhanced sensing response, with conductance modulation reaching 84–100%, whereas pristine black phosphorene shows only modest variations in the range of 4–48%. The rapid recovery at room temperature further confirms the reusability and excellent reversibility of the sensor. Overall, these findings demonstrate that Cu-decorated black phosphorene is a viable nanosensor for the selective detection of ovarian cancer-associated VOC biomarkers through breath analysis.

Received 6th April 2026,
Accepted 1st June 2026

DOI: 10.1039/d6ma00478d

rsc.li/materials-advances

1. Introduction

Ovarian cancer (OC) is a highly aggressive malignancy of the female reproductive system and represents a significant cause of cancer related deaths among women worldwide.[1,2] Despite the remarkable development of diagnostic technologies in recent decades, ovarian cancer is still primarily diagnosed at advanced stages, when treatment outcomes are severely compromised.[3] Worldwide, OC accounts for more than 324 000 new cases and over 206 000 deaths each year, and this global burden is expected to increase markedly by 2050 due to the continued growth of the ageing population.[4,5] Traditional diagnostic approaches to ovarian cancer, including pelvic ultrasound, CT imaging, and serum tumour markers, are generally invasive, expensive, and poorly sensitive for early-stage disease.[6,7] Consequently, the majority of patients are diagnosed after disease progression, at which point overall treatment outcomes are significantly poorer.[8] Breathomics, a form of breath-based molecular analysis, has recently emerged as a powerful diagnostic tool and is increasingly applied in various diseases, including cancer.[9] Accumulating data indicate that characteristic metabolic and biochemical changes occurring in ovarian cancer result in the formation of specific VOCs. These represent promising metabolic fingerprints that might enable the identification of early disease.[10] Notably, the detection of ovarian cancer-related VOCs holds great promise as a non-invasive, rapid, and low-cost diagnostic technique, which is particularly desirable for large-scale screening and point-of-care applications.[11] Thus, the development of effective nanosensors capable of selectively identifying these biomarkers is essential for timely and precise ovarian cancer diagnosis.[12]

Recent studies have shown that advances in nanoscience and nanotechnology have enabled the development of diverse low-dimensional materials, including nanosheets, nanotubes, and nanodots. Owing to their size-dependent physical and chemical properties, these materials have found widespread application in modern technologies, particularly in biomedical

Centre for Materials Sciences and Nanodevices, Department of Physics and Nanotechnology, SRM Institute of Science and Technology, Kattankulathur 603203, India. E-mail: preferec@srmist.edu.in

diagnostics and sensing.[12,13] In breath based diagnostics, volatile organic compounds (VOCs) present in exhaled breath have gained significant attention as biomarkers for the early identification of diseases. In the present study, the VOC biomarkers 2-butanone, decanal, and nonanal were selected due to their strong clinical relevance and consistent identification in ovarian-cancer-related breath studies, as reported by Sun *et al.* and Moura *et al.*[14,15] These molecules exhibit notable concentration differences between ovarian cancer patients and healthy individuals, making them reliable indicators for breath-based diagnosis. Within this series of research works, first-principles calculations have been employed to explore links between volatile organic compound (VOC) biomarkers and various diseases, including gastric cancer. The incorporation of transition metals on sensing interfaces enhances both adsorption and selectivity, and this is an evident indicator of potential for VOC-based gastric cancer detection, as reported by Ibrahim Alghoul and co-workers in 2025.[16] Using density functional theory, Narender Kumar and co-workers (2025) explored the sensing potential of pristine and metal-doped β12-borophene surfaces toward VOC biomarkers associated with Alzheimer's disease and pancreatic cancer.[17] The group showed that decoration with one Li atom can significantly improve both adsorption and selectivity, and they proposed that SAC-Li-β12-borophene could be a promising nano-biosensor material. Analyzing the diagnosis of lung cancer, Ivan Shtepliuk in 2025 conducted an extensive study on 22 VOCs related to lung cancer using DFT on graphene-based materials. The study revealed adsorption energy and charge transfer characteristics that are essential for distinguishing VOCs in AI-supported electronic noses.[18] Related to this context, L. Zhang *et al.* in 2025 employed DFT and NEGF to analyze nitrogen-doped graphyne and demonstrated physisorption-reliant sensing with high selectivity to acetone and 81% sensitivity at 0.5 V to emphasize its application in diagnosing diabetes-related VOCs.[19] The trend of support for metal functionalization persists. In addition to carbon materials, silver decoration has been identified by Janeeta Hafeez *et al.* (2024), to ensure the metallic phase of WTe_2 has a high selectivity to sense VOCs, particularly acetone, along with a highly optimal adsorption and desorption kinetics process.[20] Similarly, Wadha Alfalasi *et al.* (2024) demonstrated the selectivity and rapid recovery nature of physisorption by functionalized Ti_3C_2Tx MXene, specifically $Ti_3C_2O_2$, making it ideal. In the wider domain of metabolic diseases, the sensing of VOCs has also progressed to glucose sensing.[21] Aoly Ur Rahman and co-workers (2025) used density functional theory to investigate the adsorption behaviour of lung cancer-associated VOC biomarkers on aluminum nitride and aluminum phosphide nanotubes. They found that aluminum nitride nanotubes (AlNNT) exhibit stronger adsorption and superior electronic and thermodynamic responses, identifying AlNNT as a promising sensing material for early lung cancer diagnosis.[22] Similarly, density-functional-theory-based studies have been extended to metabolic sensing applications. For instance, Kalpana Devi *et al.* (2023) reported that metal-doped graphene, particularly Au-decorated graphene, exhibits an excellent electronic response and work-function sensitivity for glucose detection, while Ag and Cu-doped graphene also demonstrate notable sensing performance.[23] Aref Aasi and co-workers (2021) employed first-principles density functional theory to investigate the adsorption characteristics and sensing response of VOCs on pristine and Pt-decorated phosphorene. They showed that Pt decoration significantly enhances VOC phosphorene interactions, enabling highly sensitive and selective methanol detection with a short recovery time at room temperature.[24] In 2023, Jiayin Wu *et al.* used density functional theory to investigate VOC sensing on pristine and Pt-decorated SnS monolayers. They demonstrated that Pt decoration dramatically enhances charge transfer and sensitivity, while maintaining good reversibility and short recovery times, identifying Pt–SnS as a promising VOC sensing material.[25]

Motivated by previous studies, the present work employs a combined DFT and NEGF approach to investigate metal functionalized black phosphorene and evaluate its capability to adsorb three ovarian cancer related VOC biomarkers, 2-butanone, decanal, and nonanal, commonly detected in the exhaled breath of patients.[14,15,26] In the present work, density functional theory calculations are employed to investigate the interaction of 2-butanone, decanal, and nonanal molecules with metal-decorated black phosphorene. These molecules have been widely identified as VOC biomarkers in the exhaled breath of ovarian cancer patients. The adsorption behaviour is evaluated by examining variation in the structural configuration, electronic characteristics and thermodynamic properties of the metal-decorated BP nanosheets. The selectivity and sensitivity of the material towards these VOCs are also analyzed to determine its appropriateness for this purpose. The findings of this paper may help in the development of nanosensors of BP for the early diagnosis of ovarian cancer. To the best of our knowledge, a systematic theoretical or experimental study targeting the detection of these biomarkers using metal-decorated black phosphorene has not yet been reported.

2. Computational details

Density functional theory (DFT) calculation combined with the non-equilibrium greens function (NEGF) formalism were performed using the Quantum ATK simulation package (version 2024.12)[27,28] to investigate the adsorption behaviour of three OC-related VOC biomarkers, together with interfering gases (CO_2, H_2O), on black phosphorene (BP) and noble metal (Ag, Au, and Cu)-decorated BP systems. Fig. 1a depicts the orthorhombic lattice of pristine black phosphorene. To prevent artificial interactions between periodic images, a vacuum spacing of 30 Å was introduced along the y and z directions, thereby ensuring adequate isolation of the nanosheet within the simulation cell.[29] The electronic structure calculations were carried out using the generalized gradient approximation (GGA) with the Perdew–Burke–Ernzerhof (PBE) functional.[30] As GGA based methods are known to underestimate the bandgap of semiconducting systems, the Heyd–Scuseria–Ernzerhof (HSE06) hybrid functional was additionally employed to obtain a more reliable

bandgap value. In this work, HSE06 was applied specifically for band-gap evaluation, whereas the PBE functional was retained for the remaining electronic property analyses, including DOS, PDOS, and adsorption-induced electronic variations.[31] All calculations were conducted using norm-conserving pseudopotentials within the linear combination of atomic orbitals (LCAO) formalism.[32] The electronic wave functions were described using the Fritz–Haber Institute (FHI) double-zeta plus polarization (DZP) basis set, which offers a balanced compromise between computational efficiency and an accurate representation of the electronic states at a reasonable computational cost.[33] A mesh cutoff energy of 90 Hartree was selected to achieve reliable convergence of the total energy in the calculation.[34] To account for long-range dispersion interactions associated with weak physisorption, the DFT-D2 correction scheme was incorporated in the calculations.[35] Geometry optimizations were performed until the residual forces on each atom and stress in the system were reduced below 0.01 eV $Å^{-1}$ and 0.001 eV $Å^{-1}$, respectively, ensuring well-relaxed equilibrium structures.[36] In addition, the stability of noble metal (NM) incorporation (Cu, Au, and Ag) into the BP sheet was evaluated by calculating the binding energy (E_{BE}) based on total energy differences as expressed in eqn (1).[37,38]

$$E_{BE} = E_{NM@BP} - E_{BP} - E_{NM} \quad (1)$$

In this expression, the first, second, and third terms correspond to the total energies of the noble-metal-decorated BP system, pristine BP, and isolated noble metal atoms, respectively. The adsorption energy (E_{ads}) of the VOC molecules and interfering gases on the noble metal-decorated BP surface was subsequently evaluated using eqn (2).[39,40]

$$E_{ads} = E_{NM-BP/VOCs} - E_{NM-BP} - E_{VOCs} + BSSE \quad (2)$$

In this formulation, the first term corresponds to the total energy of the VOC or interfering molecule adsorbed on the NM-decorated BP surface, whereas the second and third terms represent the energies of the clean NM-decorated BP sheet, and the isolated VOC or interfering molecule, respectively. In addition to adsorption energy, sensor sensitivity is an important parameter for evaluating the performance of a VOC sensing material. The sensitivity (S) is therefore defined as the relative variation in electrical conductance of the nanosensor before and after interaction with the target VOC molecule, as expressed in eqn (3).[41,42]

$$S = \left|\frac{G_{gas} - G_{pure}}{G_{pure}}\right| \times 100 \quad (3)$$

In this relation, G_{pure} and G_{gas} represent the conductance of the pristine or noble metal-decorated BP before and after interaction with the VOC molecule, respectively. The electron-transport behaviour of the pristine and metal-decorated BP system was analysed using DFT in combination with the NEGF approach. The device model comprised left and right metallic electrodes connected through a central scattering region aligned along the z-direction. For transport calculations, the Brillouin zone was sampled using a $1 \times 3 \times 50$ Monkhorst–Pack grid. The current flowing through the device under an applied bias voltage V_b was evaluated based on the Landauer–Büttiker formalism.[43–45]

$$I = \frac{2e}{h}\int_{-\infty}^{\infty} T(E, V_b)[f(E, -\mu_L) - f_L(E - \mu_R)]dE \quad (4)$$

In this equation, $T(E)$ represents the transmission probability, $f(E)$ corresponds to the Fermi–Dirac distribution function, and E denotes the electron energy. The parameters μ_L and μ_R indicate the electrochemical potentials of the left and right electrodes, respectively. In addition, the recovery behaviour of the metal-decorated BP monolayer was estimated using the van't Hoff–Arrhenius transition-state model, as expressed in eqn (5).[46–49]

$$\tau = V_0^{-1} \exp\left(\frac{-E_{ad}}{K_B T}\right) \quad (5)$$

In this expression, E_{ads}, K_B, and T denote the adsorption energy, Boltzmann constant, and absolute temperature, respectively. The parameter V_0 represents the attempt frequency, which is typically taken as 10^{12} Hz under visible light conditions and 10^{16} Hz under ultraviolet irradiation.

3. Results and discussion

3.1. Adsorption behaviour of VOC molecules on pristine BP

The optimized structure of pristine BP, along with its electronic band structure and projected density of states (PDOS), is presented in Fig. 1(a–c). These results confirm the semiconducting nature of BP, and a GGA–PBE band gap of 0.88 eV was calculated in quite good agreement with several previous theoretical reports.[50,51] The band gap obtained with the HSE06 hybrid functional is 1.55 eV, closely matching the experimentally reported value.[52,53] While HSE06 describes the electronic structure far more accurately, its much higher computational cost makes this functional unsuitable for regular large-scale simulations.[54]

To identify the most reactive site for VOC adsorption on pristine BP, several initial configurations spanning both horizontal and vertical orientations were examined. As summarized in Table S1, the comparison of adsorption energy reveals that the horizontal configuration is the most stable; therefore, it was selected as the preferred adsorption orientation. Consequently, this configuration was chosen as the representative adsorption geometry for all subsequent investigations. Before adsorption, all VOC molecules were fully relaxed, and their optimized geometries, shown in Fig. S1 (SI), agree well with previously reported structures.[55] Afterwards, the VOC molecules were relaxed on pristine BP, as shown in Fig. 2. Among the investigated VOCs, pristine BP exhibits only moderate interaction, with the highest adsorption energy reaching −0.45 eV for the decane + BP system, while the corresponding values for all other VOCs are listed in Table 1. Overall, the adsorption strengths stay weak, especially with regard to those of common interfering air molecules. Such weak interactions signal that pristine BP is not suitable to provide reliable sensor performance. Note that an appropriate adsorption strength is a precondition to enhance sensor sensitivity. VOCs have to

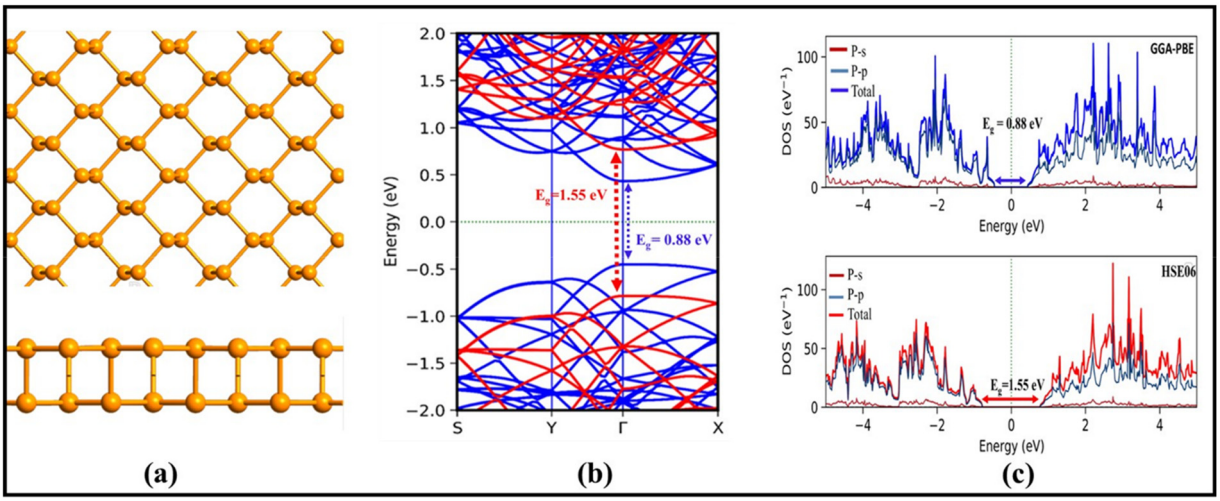

Fig. 1 Pristine black phosphorene: (a) optimized primitive-cell structure displayed from both top and lateral perspectives; (b) electronic band structure; (c) projected density of states (PDOS); the blue and red curves correspond to the GGA–PBE and HSE06 calculations, respectively.

interact sufficiently strongly with the surface to induce detectable changes in the electronic properties of the material. However, they should not interact too strongly, as desorption would then be difficult, and the sensor non-reusable. In general, the adsorption energies should lie in the regime of strong physisorption. To overcome the limitations of pristine BP and achieve adsorption in this optimal range, selected noble metals (Ag, Au, and Cu) were incorporated into BP, enabling a more favourable interaction with VOC biomarkers on the metal-functionalized BP systems, as established in our previous work.[56]

3.2. Adsorption behaviour of VOC molecules on noble metal-decorated BP

Based on the structural optimization of noble-metal-decorated black phosphorene (NMs-BP; NMs = Ag, Au, and Cu) systems previously reported by Ramkumar *et al.*,[28] the adsorption behaviour of VOC molecules on these metal functionalized BP surfaces was further investigated. After introducing the VOC molecules onto the optimized NMs–BP platforms, all configurations were fully relaxed to obtain their minimum-energy geometries. The calculated adsorption energies (Fig. 3 and Table 1) demonstrate that NMs–BP exhibits stronger interactions with the target VOC biomarkers compared with common atmospheric interfering molecules, highlighting its potential applicability for selective breath-based sensing.

Among the investigated noble-metal-decorated configurations, Cu-decorated black phosphorene (Cu@BP) exhibits the most pronounced adsorption behaviour toward the VOC molecules. In particular, Cu-decorated BP yields the strongest E_{ads} of −0.82, −0.68, and −0.65 eV for 2-butanone, decanal, and

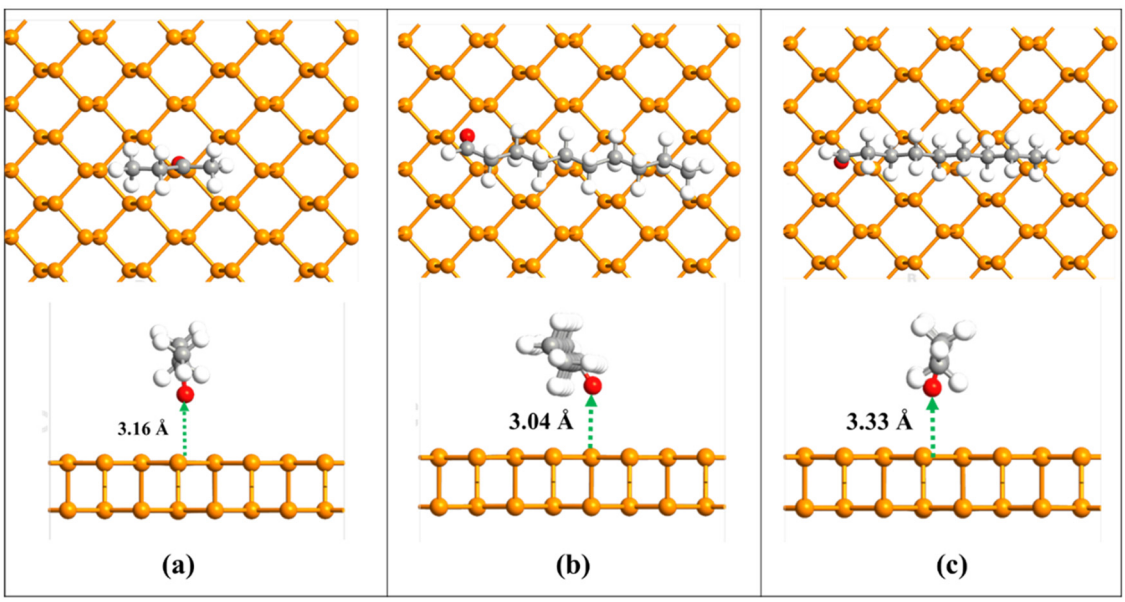

Fig. 2 Optimized adsorption configuration of OC-related VOC molecules on pristine BP (a) 2-butanone + BP, (b) decanal + BP, and (c) nonanal + BP.

Table 1 Adsorption parameters for OC-related VOC molecules and representative interfering gases on NM-decorated BP (Cu, Ag and Au): adsorption energy (E_{ads}), adsorption distance (d), band gap (E_g), charge transfer (Δq), and recovery time (τ)

System	VOCs	E_{ads} (eV)	d (Å)	E_g (eV)	Property	Δq (e)	τ (s)
Pristine	—	N/A	N/A	0.88	S/C	N/A	N/A
	2-Butanone	−0.12	3.16	0.88	S/C	0.024	1.0×10^{-10}
	Decanal	−0.45	3.04	0.87	S/C	−0.048	4.0×10^{-5}
	Nonanal	−0.13	3.33	0.87	S/C	−0.025	1.5×10^{-10}
	H_2O	0.06	3.26	0.87	S/C	0.025	1.5×10^{-14}
	CO_2	0.10	3.37	0.88	S/C	0.003	7.2×10^{-11}
Cu@BP	—	N/A	2.42	0	M	N/A	N/A
	2-Butanone	−0.82	2.04	0	M	0.189	73.86
	Decanal	−0.68	1.82	0	M	0.033	0.317
	Nonanal	−0.65	1.88	0	M	0.013	9.3×10^{-8}
	H_2O	−0.58	2.16	0	M	0.206	9.4×10^{-3}
	CO_2	−0.07	3.03	0	M	0.032	2.2×10^{-11}
Ag@BP	—	N/A	2.42	0	M	N/A	N/A
	2-Butanone	−0.67	2.34	0	M	0.165	0.215
	Decanal	−0.48	2.44	0	M	0.002	1.3×10^{-4}
	Nonanal	−0.55	2.48	0	M	0.026	2.0×10^{-3}
	H_2O	−0.46	2.44	0	M	0.166	8.8×10^{-5}
	CO_2	−0.08	3.11	0	M	0.028	3.3×10^{-11}
Au@BP	—	N/A	2.35	0	M	N/A	N/A
	2-Butanone	−0.16	3.07	0	M	0.048	2.0×10^{-10}
	Decanal	−0.25	2.96	0	M	−0.019	1.6×10^{-8}
	Nonanal	−0.41	2.62	0	M	−0.014	8.5×10^{-6}
	H_2O	−0.26	2.56	0	M	0.142	3.6×10^{-8}
	CO_2	−0.07	3.26	0	M	0.001	2.2×10^{-11}

nonanal, respectively. This enhanced interaction arises from the effective electronic coupling between the Cu active sites and the adsorbed VOC molecules, which promotes charge redistribution at the adsorption interface and strengthens the binding affinity of the sensing surface. Furthermore, the selectivity of the NM-decorated BP-based sensor was evaluated by comparing the adsorption energies of the target VOC biomarkers with those of typical atmospheric interfering gases, confirming the superior sensing capability of the Cu@BP configuration. For completeness, the corresponding adsorption characteristics of Ag and Au-decorated BP systems are presented in the SI (Fig. S2 and S3).

3.3. Electronic band structures and total density of states (TDOS) analysis

According to the adsorption analysis, the three VOC molecules – 2-butanone, decanal, and nonanal – exhibit adsorption energies greater than 1.00 eV on Cu-decorated BP, as listed in Table 1. Therefore, only these VOC molecules were considered for further investigation. The electronic structures, including the band structures, total density of states (TDOS), and optimized adsorption configurations of these VOCs on Cu-decorated BP are illustrated in Fig. 3.

Prior to VOC adsorption, the band structure and TDOS of Cu@BP (Fig. 3) clearly reveal its metallic character, with a band gap of E_g = 0 eV, as summarized in Table 1. The electronic state near the Fermi level shows strong hybridization arising from the interaction between the p orbitals of BP and the Cu-d orbitals. Upon adsorption of the VOC molecules, noticeable modifications appear in the band structures of Cu@BP, particularly around the Fermi level, indicating the formation of localized electronic states induced by the Cu decorated system. After VOC adsorption, the band structures of Cu@BP display only minor variations mainly around the Fermi level, suggesting that the interaction of the VOC molecules produces a limited perturbation to the electronic states of the system. The overall electronic behaviour can be summarized as follows: (i) the metallic nature of Cu@BP remains unchanged, although small shifts in the electronic states near the Fermi level upon adsorption of the VOC molecules are observed (see Table 1). (ii) The occupied states close to the Fermi level are still predominantly contributed by the P-orbitals of the BP lattice. In contrast, its unoccupied states retain strong contributions from the Cu (d) orbitals. These moderate VOC-induced perturbations reflect the inherent stability in the electronic structure of Cu@BP, which nevertheless allows for detectable changes in sensing. Indeed, the TDOS further supports these observations. A finite density of states remains at the Fermi level after VOC adsorption, indicating that Cu@BP retains its metallic character. Only slight variations in the TDOS are observed around the Fermi level, suggesting that the VOC molecules introduce minimal perturbation to the electronic structure. (iii) The optimised adsorption configurations displayed in Fig. 3(a–c) further illustrate different adsorption behaviours, where Fig. 3a corresponds to chemisorption, whereas Fig. 3b and c represent physisorption interactions.

3.4. Electron density difference (EDD) and electron localization function (ELF) analysis

Fig. 4 presents the EDD and ELF combined analyses for representative VOCs adsorbed on Cu-decorated black phosphorene. The EDD isosurfaces clearly evidence interfacial charge redistribution upon adsorption. Regions of electron accumulation and depletion are color-coded in green and blue, respectively. This charge redistribution is indicative of a net electron flow from the substrate Cu decorated BP toward the adsorbed VOC

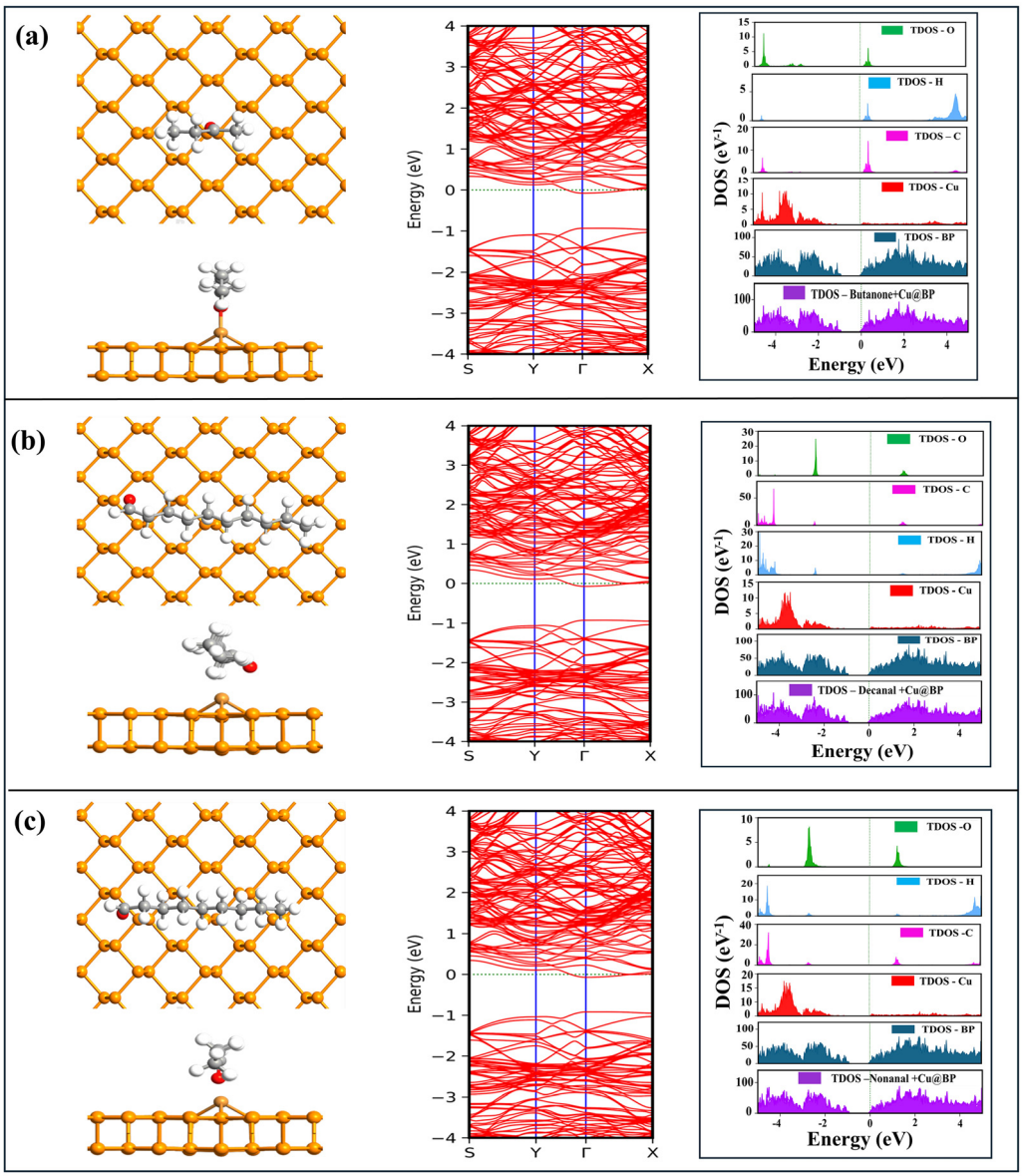

Fig. 3 Optimised adsorption geometries of OC biomarkers, on Cu-decorated BP shown from top and lateral perspectives, together with the corresponding band structure and total density of states (TDOS): (a) 2-butanone, (b) decanal, and (c) nonanal.

molecules, in good agreement with the Mulliken charge population results summarized in Table 2. The observed charge redistribution primarily originates from the Cu active sites, which contribute the dominant electronic states in the vicinity of the Fermi level. Therefore, all the studied VOCs and interfering molecules behave as electron-accepting (oxidizing) species when interacting with Cu-decorated BP. Notably, the magnitude of charge transfer correlates directly with the adsorption strength and thus confirms that enhanced interfacial electronic coupling gives rise to stronger sensor–analyte interactions. The ELF graph provides complementary insight into the nature of the bonding at the adsorption interface. For the weakly interacting VOCs, low ELF values between the adsorbate and substrate point to delocalized charge distributions typical of physisorption. For 2-butanone, however, a marked increase in the ELF localization between the oxygen atom of the molecule and the Cu site indicates the formation of a directional chemical bond. This is further corroborated by the short Cu–O bond length of 2.04 Å, as well as the largest charge transfer among the studied VOCs (Δq = 0.189e), unambiguously identifying a chemisorption mechanism. Fig. 5 presents the adsorption energies and charge transfer values for the studied VOCs and interfering molecules on Cu-decorated BP. In other words, the EDD-ELF combined analysis indicates that Cu decoration dramatically activates black phosphorene, making the effective donation of charge to VOCs possible, while the electronic interaction and selectivity are the highest for 2-butanone. These results confirm the key importance played by interfacial charge redistribution and bond formation in the performance of Cu decorated BP-based sensors toward OC VOC detection.

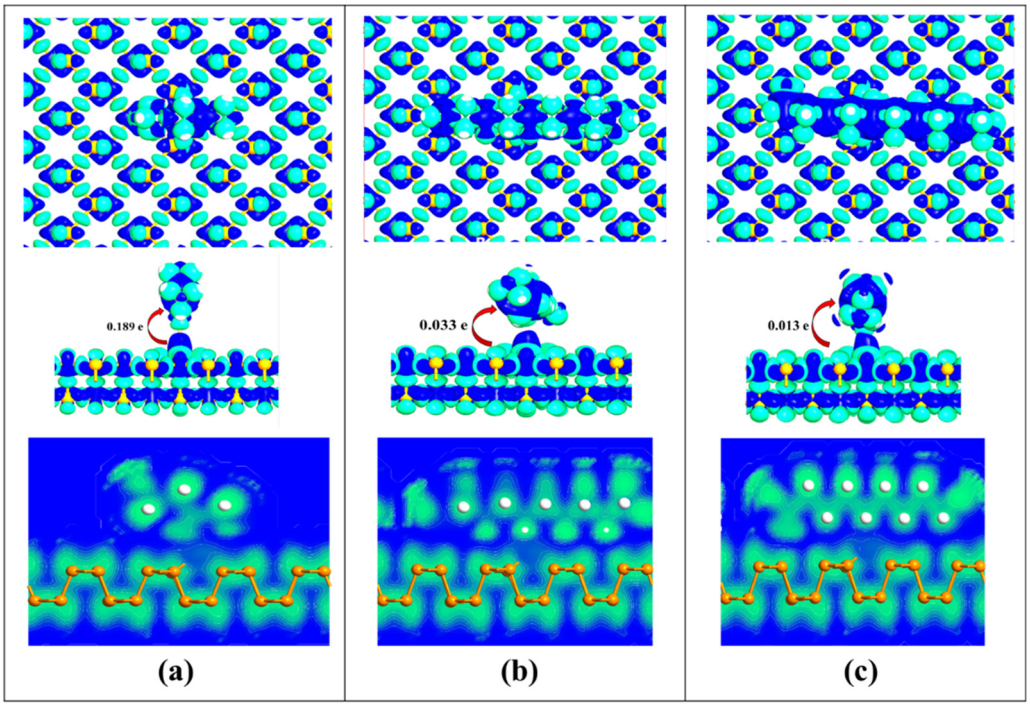

Fig. 4 Electron density difference (EDD) and electron localization function (ELF) graph illustrating the interfacial bonding characteristics of OC-related VOC molecules adsorbed on Cu decorated BP: (a) 2-butanone, (b) decanal, and (c) nonanal. Green and blue iso-surfaces indicate charge accumulation and charge depletion, respectively, with the iso-surface value set to 0.048 e Bohr^{-3}.

3.5. Recovery time

Recovery time (τ) is an important parameter that determines the reversibility of a sensing material as it reflects the desorption behaviour of the adsorbed molecules. The calculated recovery times for the target VOCs and representative interfering molecules on the Cu-decorated BP are summarized in Table 1. According to eqn (5), the recovery time is mainly determined by the adsorption energy; this implies that stronger molecule–surface interactions are typically associated with slower desorption processes. Accordingly, among the VOCs investigated, 2-butanone exhibits a comparatively strong interaction with Cu@BP, resulting in a correspondingly longer recovery time of 73.86 s. In contrast, decanal has a much shorter recovery time, amounting to 0.317 s. For nonanal, the

Table 2 Comparison of representative 2D nanomaterials reported for cancer-related VOC detection

Material	Target cancer type	VOC biomarkers	Adsorption energy range (eV)	Max sensitivity %	Recovery behavior	Ref.
Cu@BP	Ovarian cancer	2-Butanone, decanal, nonanal	−0.07 to −0.82	84–100%	Rapid 298 K	This work
N-CNR:Fe	Gastric cancer	Butanone, 2-pentanone, isoprene, pyridine methylglyoxal, *n*-decanal, and *n*-pentanal	−0.80 to −1.56	N/A	Temperature-dependent	16
Fe-WSe2	Colorectal cancer	Benzaldehyde, indole, and propan-2-ol	−0.42 to −1.26	N/A	Prolonged	57
Metal-doped β12-borophene	Alzheimer's disease and pancreatic cancer	2,3-Dimethylheptane, butylated hydroxytoluene, and pivalic acid (AD) 2-Pentanone, 4-ethyl-1,2-dimethyl benzene, and *n*-nonanol (PC)	−0.45 to −0.85	N/A	Extended	17
$Ti_3C_2T_x$ (x = O, S, F, and OH)	Lung cancer	2,3,4-Trimethylhexane, aniline, ethylbenzene, isoprene, and o-toluidine	−0.50 to −3.49	N/A	N/A	58
Ag-doped penta-PdSe2	Lung cancer	Isoprene, acrolein, isobutyraldehyde, and propan-1-ol	-1.33 to –1.72	70% to 74%	Limited	39
$Ti_3C_2T_x$ (Co, Cu, Fe, Ni)	Pancreatic cancer	2-Pentanone, 4-ethyl-1,2-dimethylbenzene, and *n*-nonanal	−0.60 to −1.10	N/A	Prolonged	59
Nitrogen-doped graphyne	Diabetes	Ethanol, ethylene glycol, acetone, and toluene	−0.29 to −0.43	81%	Rapid	19

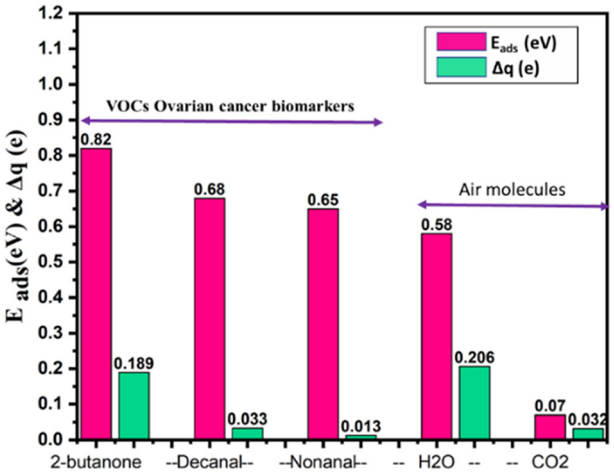

Fig. 5 Comparative overview of the adsorption energies and charge transfer values for five VOCs associated with OC biomarkers, together with representative interfering molecules interacting with Cu-decorated BP.

recovery is even faster, corresponding to ultrafast physisorption at 9.3×10^{-8} s. Similarly, this holds for typical interfering molecules like H_2O and CO_2, that desorb rapidly, with a recovery time of 9.4×10^{-3} s, while very weakly interacting species give rise to extremely low values down to 2.2×10^{-11} s. It should be noted that all recovery times were estimated at room temperature (298 K). At higher operating temperatures, the recovery time is expected to decrease considerably, resulting in values more suitable for reversible and continuous sensing applications.

4. Electronic transport properties and sensing performance

To further assess the VOC sensing capability of Cu-decorated BP, a two-probe sensor device was constructed, as schematically shown in Fig. 6(a and b). The charge transport behaviour was analysed along both the armchair and zigzag directions. In this device configuration, the left and right electrodes extend periodically along the transport (Z) direction and are directly coupled to the central scattering region. To suppress electrode-induced perturbations, a buffer region equivalent to one phosphorene layer is included at the electrode channel interfaces. The lengths of the left and right electrodes are 3.32 Å, whereas the central scattering region spans 26.56 Å. The current voltage characteristics of a Cu-decorated BP sensor during VOC desorption and adsorption were calculated using DFT-NEGF, as illustrated in Fig. 6(a–d). The electrical current (I) flowing through the Cu-decorated black phosphorene VOC sensor under a finite bias voltage (V_b) can be described using the Landauer–Büttiker formalism, as expressed in eqn (4).

When a bias voltage is applied across the electrodes of the Cu-decorated BP sensor, the Fermi level of one electrode shifts relative to that of the other electrode. Once the applied bias exceeds the threshold value, charge carriers begin to flow through the device generating an electric current. As the bias voltage increases further, the bias window becomes wider, allowing additional transmission channels to contribute to electron transport and thereby increasing the current. Adsorption of VOC molecules modifies the local electronic structure of Cu-decorated BP, which affects the transmission probability near the Fermi level and consequently alters the current response of the sensor. These adsorption-induced variations in the characteristics constitute the fundamental sensing mechanism of the Cu-decorated BP device. The sensing performance was quantified by the sensitivity, defined as the relative change in conductance induced by VOC biomarker adsorption and evaluated using eqn (3). Fig. 6 presents the conductance (I/V) behaviour for the different configurations. Based on these results, the sensing sensitivity was evaluated for both the armchair and zigzag transport directions for pristine and Cu-decorated BP under bias voltages ranging from 0 to 3 V. The sensitivity comparison for pristine and Cu-decorated BP is illustrated in Fig. 7, where the armchair direction at a bias voltage of 0.6 V and the zigzag direction at 2.0 V are considered. At 0.6 V in the armchair direction (Fig. 7a), pristine BP exhibits sensitivities of 11% for 2-butanone, 4% for decanal, 7% for nonanal, 12% for H_2O, and 12% for CO_2. Under the same conditions, Cu-decorated BP shows significantly enhanced sensitivities of 61% for 2-butanone, 36% for decanal, and 46% for nonanal. Likewise, in the zigzag direction at a bias voltage of 2.0 V (Fig. 7b), pristine BP demonstrates sensitivities of 16% for 2-butanone, 17% for decanal, 14% for nonanal, 4% for H_2O, and 48% for CO_2. In contrast, Cu-decorated BP exhibits much higher sensitivities of 91% for 2-butanone, 100% for decanal, and 84% for nonanal.

Overall, Cu decoration significantly enhances the sensing response in both transport directions, and the armchair direction exhibits a notable improvement in sensitivity compared to pristine BP. However, the zigzag direction exhibits a significantly stronger and more pronounced response, with higher sensitivity values for all target VOCs. This indicates that although both directions are suitable for sensing applications, charge transport along the zigzag orientation is more effectively modulated by VOC adsorption, making the zigzag direction the most favourable configuration for achieving optimal sensing performance in the Cu-decorated BP sensor.

Compared with previously reported two-dimensional sensing materials for cancer-related VOC detection, Cu-decorated BP exhibits a favourable balance between adsorption strength and electronic response at room temperature (Table 2). Many sensing platforms either suffer from excessively strong adsorption, leading to slow recovery, or from weak interactions that result in minimal conductance modulation. In contrast, the Cu@BP system demonstrates an optimal interaction strength with VOC biomarkers, enabling significant charge transfer and pronounced conductance variation while maintaining rapid desorption characteristics. This balanced adsorption–desorption behaviour demonstrates that Cu@BP has strong potential as an effective nanosensor for the rapid and non-invasive detection of ovarian cancer biomarkers.

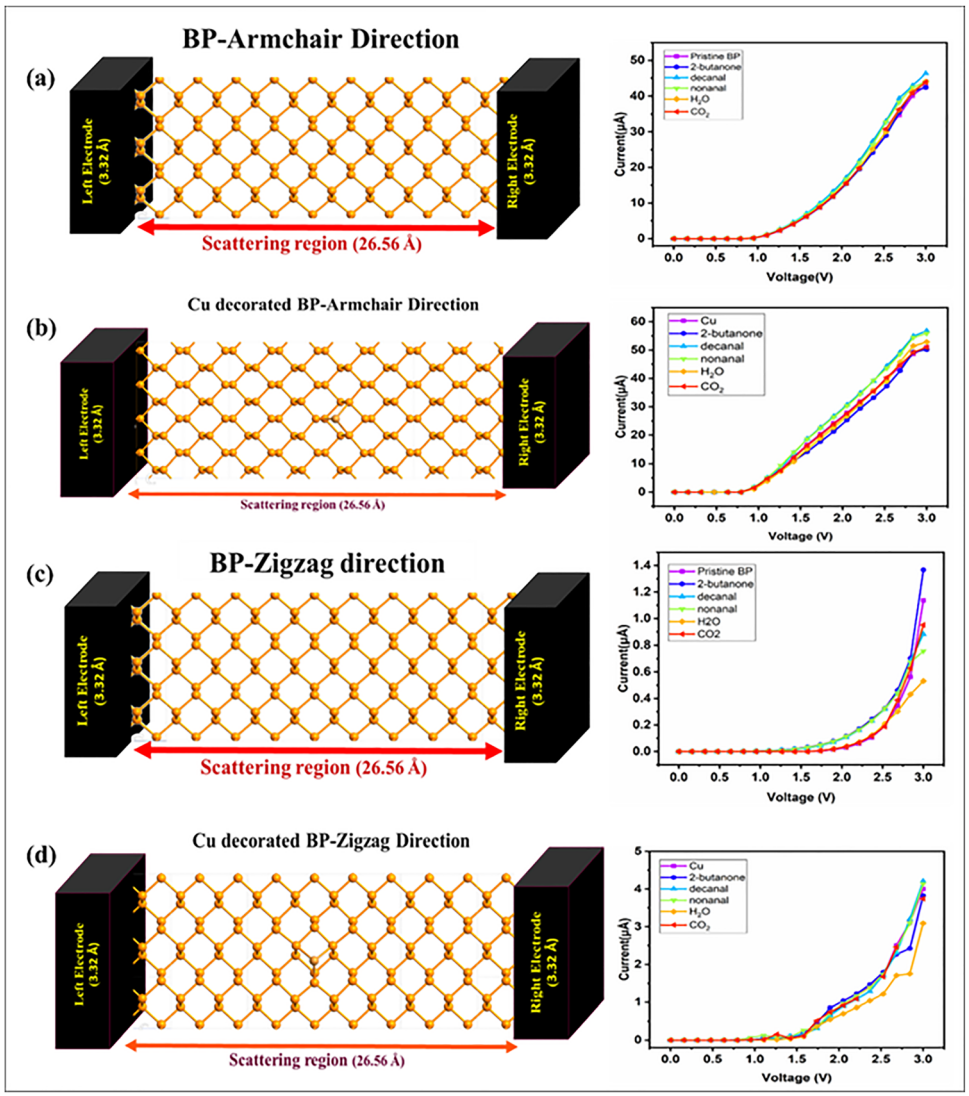

Fig. 6 Two-probe device configuration and corresponding current–voltage (*I*/*V*) characteristics of BP along different crystallographic orientations. The transport responses are presented for (a) pristine BP and (b) Cu-decorated BP in the armchair direction, and for (c) pristine BP and (d) Cu-decorated BP in the zigzag direction, highlighting the influence of Cu functionalization and the intrinsic anisotropy of BP on charge-transport behaviour.

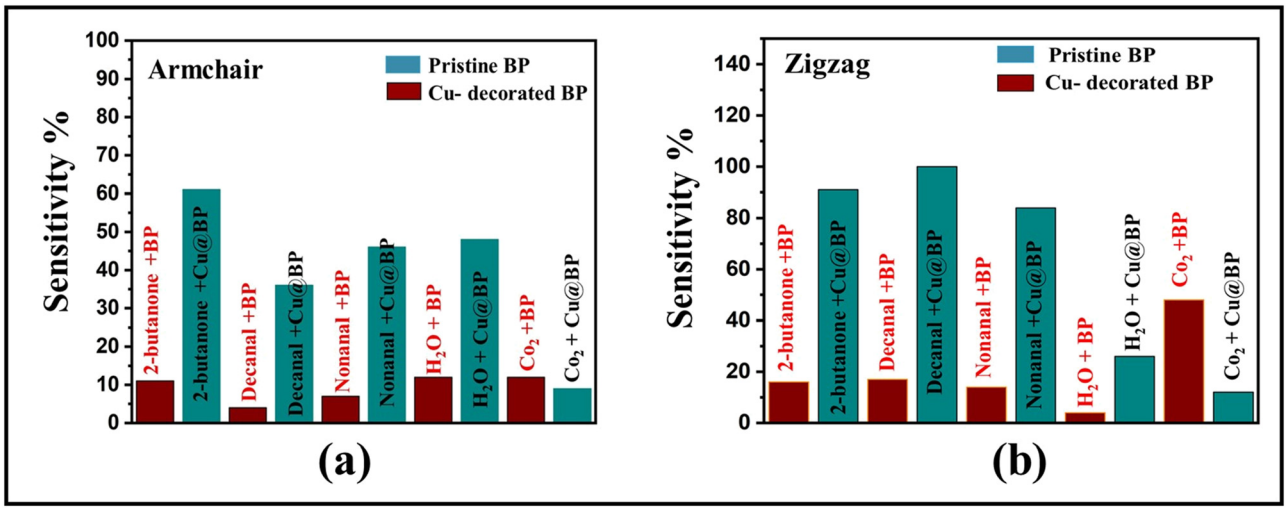

Fig. 7 Comparison of the sensing sensitivity of pristine BP and Cu@BP toward VOC biomarkers along the (a) armchair and (b) zigzag directions.

5. Conclusion

In this study, density functional theory calculations were performed to examine the adsorption behaviour of three OC related VOC biomarkers in comparison with two interfering molecules (CO_2, H_2O) on pristine and metal-decorated BP. The adsorption of the VOCs on pristine black phosphorene yielded weak interaction energies, indicating low sensing capability. To improve the adsorption mechanism and selectivity, the selected NMs (Au, Ag, and Cu) were introduced into the black phosphorene surface. Among the decorated systems, Cu-decorated black phosphorene exhibits the most pronounced improvement, yielding strong E_{ads} values of −0.82, −0.68, and −0.65 eV for 2-butanone, decanal, and nonanal, respectively, thereby confirming its superior sensing capability. The *I–V* characteristics clearly indicate that Cu-decorated BP exhibits a substantially stronger sensing signal, achieving conductance variations in the range of 84–100%, whereas pristine BP shows only modest changes confined to the 4–48% range. The recovery time analysis indicates fast desorption for 2-butanone (73.86 s), decanal (0.317 s), and nonanal (9.3×10^{-8} s) at 298 K, highlighting the excellent reversibility and reusability of the Cu decorated BP sensor. Overall, these results authenticate Cu-decorated black phosphorene as a robust and efficient nanosensing platform for the selective detection of ovarian cancer related VOC biomarkers, offering strong potential for non-invasive breath-based diagnostic applications.

Author contributions

All authors of this manuscript contributed to this research study. D. Ramkumar: conceptualization, data curation, and writing – original draft. K. A. Jeeva Vergin Raj: data curation, formal analysis, and visualization. N. Viveka: methodology and validation. C. Preferencial Kala: visualization, supervision, and writing – review & editing. R. M. Hariharan: visualization, formal analysis, and data curation.

Conflicts of interest

The authors declare that they have no known competing financial interests or personal relationships that could have appeared to influence the work reported in this paper.

Data availability

The data that support the research findings of this study are not publicly available due to confidentiality of the information, data protection, and privacy, but they can be provided upon reasonable request through the proper channel.

Supplementary information (SI) contains additional adsorption studies on Ag@BP and Au@BP nanosheets. See DOI: https://doi.org/10.1039/d6ma00478d.

Acknowledgements

The authors gratefully acknowledge the financial support provided by the DST-FIST, Government of India (Ref. No. SR/FST/PSI-155/2010). The authors convey their special thanks to the High-Performance Computing Center, SRMIST, for providing the computational facility and to all their beloved teammates.

References

1 U. A. Matulonis, A. K. Sood, L. Fallowfield, B. E. Howitt, J. Sehouli and B. Y. Karlan, *Nat. Rev. Dis. Primers*, 2016, **2**, 16061.
2 G. C. Jayson, E. C. Kohn, H. C. Kitchener and J. A. Ledermann, *Lancet*, 2014, **384**, 1376–1388.
3 K. R. Cho and I.-M. Shih, *Annu. Rev. Pathol.: Mech. Dis.*, 2009, **4**, 287–313.
4 G. Caruso, S. J. Weroha and W. Cliby, *JAMA*, 2025, **334**, 1278.
5 F. Raspagliesi, G. Bogani, S. Benedetti, S. Grassi, S. Ferla and S. Buratti, *Cancers*, 2020, **12**, 2408.
6 Y. Chen, W. Jiang, Y. Zhang, D. Chen, M. Xu, J. Liu and P. Jia, *Colloids Surf., A*, 2025, **722**, 137289.
7 Z. Jia, Y. Jiang, T. Shang, H. Cao, J. Li, L. Cong, P. Pu, H. Xu, Y. Liu, Y. Huang, D. Ma, J. Wu, R. Zhou, X. Wang, C. B. Han and J. Liu, *J. Nanobiotechnol.*, 2025, **23**, 468.
8 M. Boeri, S. Sestini, O. Fortunato, C. Verri, P. Suatoni, U. Pastorino and G. Sozzi, *Expert Rev. Mol. Diagn.*, 2015, **15**, 801–813.
9 B. Sharma, B. Chettri, P. Karki, S. K. Das, P. Chettri and A. Rao, *Surf. Interfaces*, 2026, **80**, 108339.
10 A. Wilson, *Metabolites*, 2015, **5**, 140–163.
11 N. Nasiri and C. Clarke, *Sensors*, 2019, **19**, 462.
12 H. Cheng, R. Chen, Y. Zhan, W. Dong, Q. Chen, Y. Wang, P. Zhou, S. Gao, W. Huang, L. Li and J. Feng, *Anal. Chem.*, 2024, **96**, 18555–18563.
13 D. Tyagi, H. Wang, W. Huang, L. Hu, Y. Tang, Z. Guo, Z. Ouyang and H. Zhang, *Nanoscale*, 2020, **12**, 3535–3559.
14 P. C. Moura, M. Raposo and V. Vassilenko, *Biomed. J.*, 2023, **46**, 100623.
15 X. Sun, K. Shao and T. Wang, *Anal. Bioanal. Chem.*, 2016, **408**, 2759–2780.
16 I. Alghoul, T. Hussain, S. Nazir and N. Tit, *Sci. Rep.*, 2025, **15**, 13173.
17 N. Kumar, K. Thakur, P. Ranjan, A. Kumar and N. Tit, *Surf. Interfaces*, 2025, **60**, 106072.
18 I. Shtepliuk, D. Puglisi and J. Eriksson, *Appl. Surf. Sci.*, 2025, **696**, 162985.
19 L. Zhang, B. He, Y. Li, J. Yun, L. Yao, H. Zhao, J. Yan, W. Zhao and Z. Zhang, *ACS Sens.*, 2025, **10**, 2499–2509.
20 J. Hafeez, M. Usama Islam, S. M. Ali, S. Khalid, N. Ashraf and M. I. Khan, *Mater. Sci. Semicond. Process.*, 2024, **182**, 108710.
21 W. Alfalasi, T. Hussain and N. Tit, *Sci. Rep.*, 2024, **14**, 1403.
22 A. U. Rahman, D. M. Saaduzzaman, S. M. Hasan, M. Amin and Md. K. U. Sikder, *Sci. Rep.*, 2025, **15**, 34852.
23 K. P. Devi and K. K. Singh, *Biosens. Bioelectron.:X*, 2023, **13**, 100287.

24 A. Aasi, S. M. Aghaei and B. Panchapakesan, *J. Mater. Chem. C*, 2021, **9**, 9242–9250.
25 J. Wu, Z. Li, A. Luo and X. Xing, *Sensors*, 2023, **23**, 7319.
26 P. Mochalski, M. Leja, D. Ślefarska-Wolak, L. Mezmale, V. Patsko, C. Ager, A. Królicka, C. A. Mayhew, G. Shani and H. Haick, *Diagnostics*, 2023, **13**, 335.
27 S. Smidstrup, T. Markussen, P. Vancraeyveld, J. Wellendorff, J. Schneider, T. Gunst, B. Verstichel, D. Stradi, P. A. Khomyakov, U. G. Vej-Hansen, M.-E. Lee, S. T. Chill, F. Rasmussen, G. Penazzi, F. Corsetti, A. Ojanperä, K. Jensen, M. L. N. Palsgaard, U. Martinez, A. Blom, M. Brandbyge and K. Stokbro, *J. Phys.: Condens. Matter*, 2020, **32**, 015901.
28 D. Ramkumar, K. A. Jeeva Vergin Raj, C. Kala and R. Hariharan, *Surf. Interfaces*, 2025, **76**, 107944.
29 R. Bhuvaneswari and R. Chandiramouli, *Chem. Phys. Lett.*, 2018, **701**, 34–42.
30 J. P. Perdew, K. Burke and M. Ernzerhof, *Phys. Rev. Lett.*, 1996, **77**, 3865–3868.
31 J. Heyd and G. E. Scuseria, *J. Chem. Phys.*, 2004, **121**, 1187–1192.
32 J. F. Mulligan, *J. Chem. Phys.*, 1951, **19**, 347–362.
33 A. Aasi, S. M. Aghaei and B. Panchapakesan, *J. Mater. Chem. C*, 2021, **9**, 9242–9250.
34 W. Yu, Z. Zhu, C.-Y. Niu, C. Li, J.-H. Cho and Y. Jia, *Phys. Chem. Chem. Phys.*, 2015, **17**, 16351–16358.
35 S. Grimme, *J. Comput. Chem.*, 2006, **27**, 1787–1799.
36 P. Lakhera, S. Singh, R. Mehla, V. Chaudhary, P. Kumar and S. Kumar, *IEEE Sens. J.*, 2022, **22**, 7572–7579.
37 I. Alghoul, W. Othman, I. Abdi, T. Hussain and N. Tit, *Results Phys.*, 2025, **78**, 108493.
38 M. Mushtaq, I. Muhammad, Z. Chang, Z. Leilei, M. A. R. Khan, N. Rahmani, A. Shabani, H. Bae, H. Lee and T. Hussain, *FlatChem*, 2024, **48**, 100764.
39 B. Sharma, B. Chettri, P. Karki, S. K. Das, P. Chettri and A. Rao, *Surf. Interfaces*, 2026, **80**, 108339.
40 H. Ahmad, X. Li, B. A. Kalwar, X. Tan and M. R. Naich, *Chem. Phys.*, 2025, **589**, 112522.
41 L. Lin, X. Li, C. Xue, X. Cai, H. Tao and Z. Zhang, *Langmuir*, 2023, **39**, 15142–15151.
42 G. Fan, X. Wang, X. Tu, H. Xu, Q. Wang and X. Chu, *Nanotechnology*, 2021, **32**, 075502.
43 P. Kumar, B. Kumar and S. Kumar, *Electron. Struct.*, 2025, **7**, 035003.
44 R. Bhuvaneswari, J. P. Maria, V. Nagarajan and R. Chandiramouli, *Chem. Phys. Lett.*, 2020, **747**, 137353.
45 Y. Xue, S. Datta, S. Hong, R. Reifenberger, J. Henderson and C. Kubiak, *Phys. Rev. B: Condens. Matter Mater. Phys.*, 1999, **59**, R7852–R7855.
46 P. Ou, P. Song, X. Liu and J. Song, *Adv. Theory Simul.*, 2019, **2**, 1800103.
47 S. M. Aghaei, A. Aasi, S. Farhangdoust and B. Panchapakesan, *Appl. Surf. Sci.*, 2021, **536**, 147756.
48 S. Peng, K. Cho, P. Qi and H. Dai, *Chem. Phys. Lett.*, 2004, **387**, 271–276.
49 I. G. Pitt, R. G. Gilbert and K. R. Ryan, *J. Phys. Chem.*, 1994, **98**, 13001–13010.
50 S. Y. Lei, Z. Y. Yu, H. Y. Shen, X. L. Sun, N. Wan and H. Yu, *ACS Omega*, 2018, **3**, 3957–3965.
51 A. Aasi, S. M. Aghaei and B. Panchapakesan, *J. Mater. Chem. C*, 2021, **9**, 9242–9250.
52 D. Çakır, H. Sahin and F. M. Peeters, *Phys. Rev. B: Condens. Matter Mater. Phys.*, 2014, **90**, 205421.
53 D. Guedes-Sobrinho, C. R. Caldeira Rêgo, G. R. Da Silva, H. R. Da Silva, W. Wenzel, M. J. Piotrowski and A. Cavalheiro Dias, *J. Phys. Chem. C*, 2024, **128**, 7242–7251.
54 J. Heyd, G. E. Scuseria and M. Ernzerhof, *J. Chem. Phys.*, 2003, **118**, 8207–8215.
55 A. Amann, W. Miekisch, J. Schubert, B. Buszewski, T. Ligor, T. Jezierski, J. Pleil and T. Risby, *Annual Rev. Anal. Chem.*, 2014, **7**, 455–482.
56 D. Ramkumar, R. Akash, C. Preferencial Kala and D. John Thiruvadigal, *ECS J. Solid State Sci. Technol.*, 2025, **14**, 117001.
57 T. Hussain, H. Bae, Y. Pal, P. Panigrahi, S. Nazir, M. Naher, A. Assen and H. Lee, *Langmuir*, 2025, **41**, 13134–13143.
58 P. Panigrahi, H. Vovusha, Y. Pal, H. Bae, H. Lee, T. Kaewmaraya, S. Nazir, M. J. A. Shiddiky and T. Hussain, *ACS Appl. Nano Mater.*, 2023, **6**, 22117–22127.
59 N. Kumar, T. Hussain, L. Shen, Y. P. Feng and N. Tit, *Results Phys.*, 2025, **75**, 108346.